Chinese Chemical Letters 35 (2024) 108948

Contents lists available at ScienceDirect

Chinese Chemical Letters

journal homepage: www.elsevier.com/locate/cclet

Intelligent design and construction of novel APN-based theranostic probe driven by advanced computational methods

Yingli Zhu[a], Jie Qian[b], Kunqian Yu[c], Jing Hou[a], Yeshuo Ma[d], Fei Chen[a], Jie Dong[a,*], Wenbin Zeng[a,*]

[a] Xiangya School of Pharmaceutical Sciences, Central South University, Changsha 410083, China
[b] National Engineering Research Center of Rice and Byproduct Deep Processing, School of Food Science and Engineering, Central South University of Forestry and Technology, Changsha 410004, China
[c] State Key Laboratory of Drug Research, Drug Discovery and Design Center, Shanghai Institute of Materia Medica, Chinese Academy of Sciences, Shanghai 201203, China
[d] Department of Geriatrics, Third Xiangya Hospital, Central South University, Changsha 410013, China

ARTICLE INFO

Article history:
Received 11 July 2023
Revised 17 August 2023
Accepted 18 August 2023
Available online 19 August 2023

Keywords:
Theranostic probe
Artificial intelligence
Conformational restriction
Fluorescence restoration
Design strategy

ABSTRACT

Multifunctional molecules with both optical signal and pharmacological activity play an important role in drug development, disease diagnosis, and basic theoretical research. Aminopeptidase N (APN), as a representative tumor biomarker with anti-tumor potential, still lacks a high-precision theranostic probe specifically targeting it. In this study, a novel quaternity design strategy for APN theranostic probe was developed. This proposed strategy utilizes advanced machine learning and molecular dynamics simulations, and cleverly employs the strategy of conformation-induced fluorescence recovery to achieve multi-objective optimization and integration of functional fragments. Through this strategy, a unique "Off–On" theranostic probe, **ABTP-DPTB**, was ingeniously constructed to light up APN through fluorescence restoration, relying on conformation-induced effects and solvent restriction. Differ from the common diagnostic probes, the intelligent design with non-substrated linkage makes **ABTP-DPTB** for long-term *in-situ* imaging. The fabricated probe was used for detecting and inhibiting APN in various environments, with a better *in vitro* inhibitory than golden-standard drug bestatin.

Multifunctional molecules with both optical signal and targeting groups play an important role in drug development, disease diagnosis, and basic theoretical research. Among them, theranostic probes combine diagnostic and therapeutic capabilities into a single agent, enabling targeted delivery of therapy and real-time monitoring of treatment response. Malignant tumor is a significant public health problem worldwide [1] with the changelings of insidious onset, difficult diagnosis, and limited treatment option. Aminopeptidase N (APN), is an over-expressed enzyme in numerous malignancies [2–6], and can promote cancer development through various pathways [7–11]. Detecting and inhibiting APN is crucial for the diagnosis and treatment of cancer and cancer-related inflammation [12–18]. The development of an APN targeting theranostic probe is of great significance for achieving precise, real-time, and dynamic diagnosis and targeted treatment of cancer.

In recent years, many cancer inhibitors [19,20] and detection methods [21–30] based on APN have been developed. However, most of classical diagnostic probes do not possess therapeutic functions, and still have a series of unavoidable deficiencies [31–33]. The main reason is that the principle of hydrolysis of N-terminal Ala residues of the polypeptide by APN was adopted as the response mechanism in all these probes, resulting in their luminescent properties having an irreversible "Turn-On" characteristic [34–39]. When such probes respond, their fluorophores become completely embedded in APN, which blocks the optical signals. When these fluorophores are released due to the conformational change of APN, their ability for *in-situ* imaging is significantly reduced. Besides, due to the use of the same catalytic substrate, most fluorescent probes based on enzymatic hydrolysis reaction cannot distinguish different isoenzymes, which may lead to false positive results [40]. The main drawbacks of these traditional probes are mostly caused by neglecting the structural characteristics of the receptor and the kinetics of the response process in the design process. Therefore, it is particularly important to develop a system-

* Corresponding authors.
E-mail addresses: jiedong@csu.edu.cn (J. Dong), wbzeng@hotmail.com (W. Zeng).

https://doi.org/10.1016/j.cclet.2023.108948
1001-8417/

atic design strategy integrates information of the receptor and the properties of the probe.

Recently, artificial intelligence has been widely used in drug development, including target prediction [41], virtual screening [42], property prediction [43], drug repurposing, *etc*. Molecular docking and molecular dynamics (MD) simulation are also acknowledged as the powerful tools in the field of receptor-based drug design. At the same time, a novel strategy based on excited state intramolecular proton transfer (ESIPT) is often used to construct fluorophores with tunable emissions. ESIPT is the internal proton transfer phenomenon that occurs within a single excited molecule [44–46]. Compared with common fluorophores, the ESIPT fluorophore has a large stokes shift, which can effectively shield the influence of self-absorption [47–50].

This study provides a novel quaternity design strategy for APN theranostic probes: (1) Using machine learning (ML) to screen for high-affinity targeted inhibitor fragments to ensure that the designed probe has expectant activity. (2) By utilizing interpretation of ML and structure–activity relationship (SAR) analysis, combined with the structural information of the receptor, a novel ESIPT fluorescent has been screened. (3) Using molecular simulation and the conformational restriction strategy based on the specific receptor, flexible linkers were screened and optimized. Ensuring that the photo-induced electron transfer (PET) effect between the pharmacophore and the fluorophore is terminated during the response, in order to achieve precise long-term *in-situ* imaging. (4) Chemical synthesis, optical characterization, and *in vitro* experiments were further verified that the constructed APN probe possesses the expectant diagnostic and therapeutic properties. This quaternity design strategy can overcome the problems caused by traditional design strategies, such as inadequate targeting, lack of long-term *in situ* imaging capability, and inability to achieve reversible sensing. More importantly, it provides a systematic reference method for the development of other receptor-based theranostic probes.

To be specific, firstly, to effectively isolate the solvent's influence on the fluorophore and prevent the fluorescence signal from being embedded inside the protein, the final binding conformation of the probe based on the structure of APN has been designed. When APN is activated, the binding site is encased in a special large cavity (2800 $Å^3$), which is mainly composed of residues from domain II (336 $Å^2$) and domain IV (134 $Å^2$) [3]. There are three channels that extend from the cavity to the outside, with the one closest to the outside defined as pipe D4. The outer side of pipe D4 has a unique structure similar to a funnel. And in this work, the spatial structure of APN was used to gradually generate and assemble functional fragments, allowing the ideal binding conformation of the designed probe to stably exist inside the receptor. Secondly, in order to achieve a strong binding between the probe and APN, and to ensure the probe has pharmacological activities, a targeting inhibitory fragment with high-affinity was screened out through ML. By considering both the model's interpretation and the surface shape of Pipe D4, a novel ESIPT fluorophore was designed and screened out. Furthermore, to avoid the limitation of traditional probes and achieve recyclable long-term *in situ* imaging, the conformation-induced mechanism was utilized to construct a novel "Off–On" probe. Using a flexible linker to connect the fluorophore and the pharmacophore, allows them to stack in a solvent environment, resulting in PET effect and fluorescence quenching. Based on this, the pharmacophore and fluorophore were further integrated by repeatedly screening the length of the flexible linker to fit the shape of Pipe D4. The applicable linker ensures the firmly combination between pharmacophore and the Zn^{2+} in the active site, and allows the fluorophore to pass through pipe D4. As the probe is stretched and fixed in APN, the pharmacophore and fluorophore become separated, terminating the PET effect and restoring fluorescence emission. Further verification through chemical synthesis, optical characterization, and *in vitro* experiments confirmed that the constructed APN probe possesses expected diagnostic and therapeutic properties.

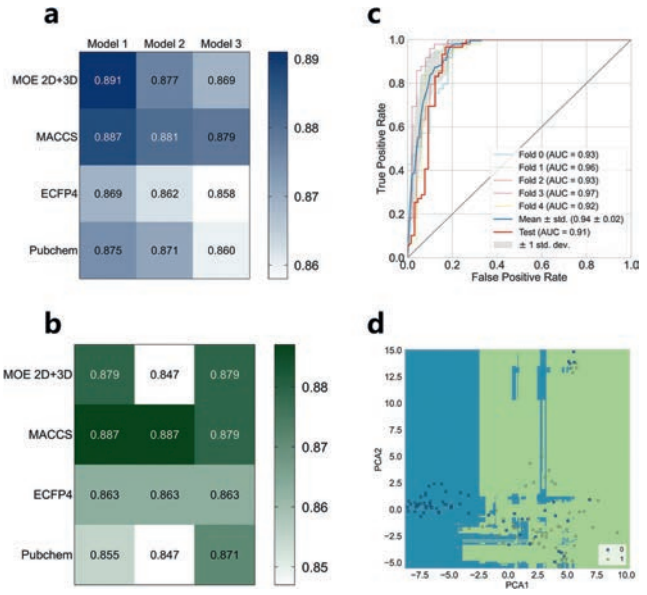

Fig. 1. The constructed ML models for APN inhibitor prediction. (a) The heatmaps of top 3 algorithms with the best performance among different characterization methods in 5-fold CV. Models 1 to 3 respectively represent the different algorithms based on MOE 2D+3D (ET, XGBoost, RF), ECFP4 (GBT, CatBoost, RF) and Pubchem (LightGBM, CatBoost, RF). (b) The heatmaps of top 3 algorithms with the best performance among different characterization methods in the test set. Model 1 to 3 represent the same algorithms as a. (c) Receiver operating characteristic (ROC) curve for CV and test of MACCS-LightGBM model. The AUC of the ROC curve was 0.94 ± 0.02 in 5-fold CV and 0.91 in the test set. (d) Decision boundary of MACCS-LightGBM model. The feature information was compressed into two principal components, and the prediction category was obtained by predicting the coordinates of each small grid. Scatter is the real category distribution in the test set.

In order to obtain the potential structure of inhibiting APN, twelve machine learning algorithms were employed to build models with Molecular Operating Environment (MOE) descriptors, MACCS fingerprint, ECFP4 fingerprint and PubChem fingerprint and tested *via* 5-fold cross-validation (CV). The top three algorithms with the best performance were used to construct the prediction model (Table S1 in Supporting information). The LightGBM models using MACCS fingerprints (MACCS-LightGBM) achieved the best prediction accuracy (ACC) ($ACC_{test} = 0.887$, Fig. 1b) as well as satisfactory performance in CV ($ACC_{cv} = 0.887$, Fig. 1a). Therefore, MACCS-LightGBM model was finally selected (Figs. 1c and d) for the screening of APN inhibitors. In order to explore the relationship between the chemical structure and effectiveness of the APN inhibitors, MACCS-LightGBM model was further interpreted based on SHapley Additive exPlanations (SHAP) and the feature importance of LightGBM model (Figs. S1 and S2 in Supporting information). Among the top 20 most important features determined by feature importance and SHAP, a total of 13 common features were found. Among them, MACCS156 is considered by SHAP as the most important substructure for the model, and it also has a favorable ranking in the feature importance rating (rankFI = 13).

In order to select the functional fragments and construct the optical component, the six suggested structures were obtained by using MOEsaic. The ZINC database (https://zinc20.docking.org/) was used to search the similar structures of these suggested structures. Then, the top 200 similar structures were obtained and then added to the inhibitor library (lib_In). On the basis of empirical design and literature survey, a total of 55 novel fluorophores

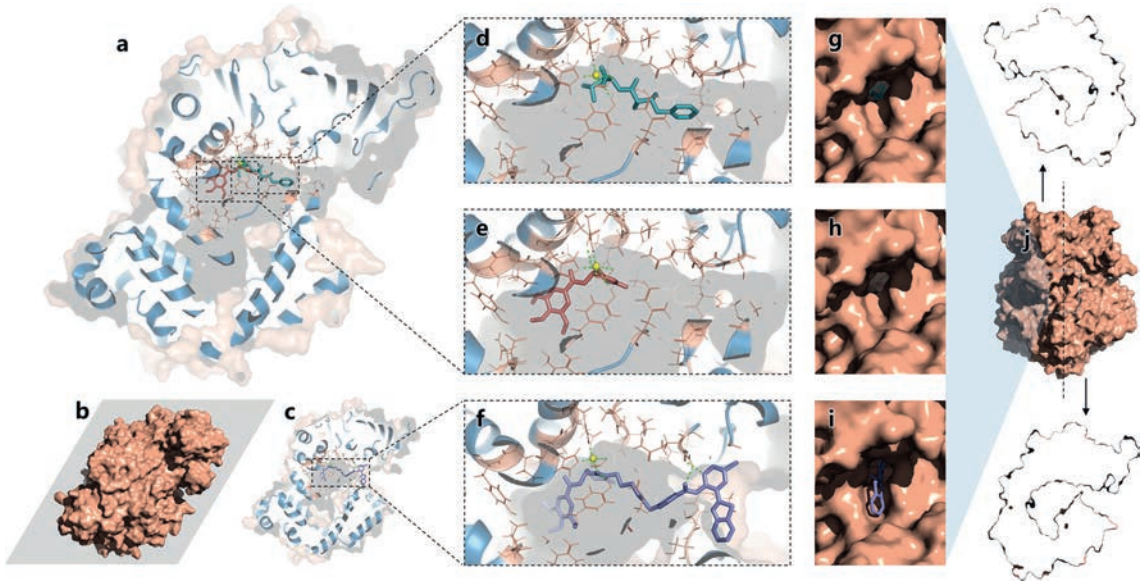

Fig. 2. Molecular docking guided the construction of **ABTP-DPTB**. (a, c) Cross-sectional view of APN binding with different ligands. (b) The position of the cross-section. (d–f) Different binding modes of bestatin (cyan), **DPTB** (wheat) and **ABTP-DPTB** (purple) to the active site of APN. (g–i) The outside view of corresponding ligands in pipe D4. (j) The surface map and open-book view of pipe D4 in APN.

were used to construct the database of the signal component (lib_S). The top 50 positive structures (probability >0.99) were filtrated from lib_In *via* MACCS-LightGBM model as potential inhibitors. Further, molecular docking of these potential inhibitors was performed to screen for structures with the expected unique binding form to APN. Under these conditions, fragments *N*-(2,6-dioxopiperidin-3-yl)-3,4,5-trimethoxybenzamide (**DPTB**, predicted probability = 0.9946) was selected to be the optimal fragment with modifiable sites and in the same direction as pipe D4. Combined with the model interpretation results, it can be found that **DPTB** not only has the most influential substructure MACCS156, but also has several important structural features (MACCS148, 151, 159, 164, Fig. S2 in Supporting information). In addition, the predicted properties of **DPTB** screened by ADMETlab [43] were similar to bestatin (Figs. S3 and S4 in Supporting information), suggesting that it may have considerable effects *in vivo*. In the design of optical components, considering both the interpretation of the MACCS model and the shape of the outer surface of pipe D4, an unreported novel pyridinium fluorophore fragment of *N*-(2-(benzo[*d*]thiazol-2-yl)-4-chlorophenyl)isonicotinamide (**ABTP**) was constructed. Surprisingly, when fed into the MACCS-LightGBM model, **ABTP** showed outstanding predictive activity (0.8573) compared with the other designed fluorophores (lib_S), most of which have been reported in recent years.

Next, **DPTB** and **ABTP** were spliced step by step under the guidance of molecular docking. The redocking between bestatin and APN overlapped well with the experimental crystal structure (Figs. 2a and b), indicated that the proposed molecular docking model is accurate (Fig. S5 in Supporting information). Compared with bestatin (Figs. 2d and g), **DPTB** showed the strength of being able to bind to the active site of APN in a more unique pose. There was adequate modifiable space next to **DPTB** when it bound to APN (Fig. 2e), which provided the possibility of splicing signal components. We were surprised to find that the modifiable site of **DPTB** was oriented just in the same direction as the trajectory of pipe D4 after binding to APN (Figs. 2e and h), which led to the external environment of APN (Fig. 2j). This phenomenon indicated that the selected signaling component has the potential to cross the pip D4 and reach the external of the APN under a reasonable design.

However, when bound to APN, the modification space around bestatin is very limited (Fig. 2d). Moreover, in the binding conformation, bestatin will block pipe D4 from the front (Figs. 2d and g). If bestatin is chosen as the pharmacophore, the fluorophore will be embedded in the internal cavity of APN, and effective optical signal will be blocked. Besides, the modifiable site -COOH of bestatin, is also a functional group that interacts with Zn^{2+} in APN. The modification of this site will probably reduce the pharmacological activity of bestatin. On the contrary, **DPTB** has a proper site with the idea orientation, which does not participate in the interaction between **DPTB** and Zn^{2+}. Modifying **DPTB** at this site theoretically has little adverse effect on pharmacological activity.

On this basis, we further screened the appropriate linkers for assembling **DPTB** and **ABTP**, to make full use of the structural specificity of pipe D4 and construct a conformational sensitive probe. The docking results showed that the fluorophore **ABTP** can act on the terminal of pipe D4 in the most suitable way when the linker consists of six carbon atoms (Table S3 in Supporting information). In this case, the benzothiazoles in **ABTP** fit neatly into the rectangular funnel at the terminal of pipe D4. This binding conformation makes the intramolecular hydrogen bonds involved in ESIPT toward the inner side of the protein. Thus, the adverse effects of the solvent are expected to be eliminated (Figs. 2c, f and i). At this time, **ABTP** is firmly anchored to the terminal of pipe D4 which is in the shape of "7", which makes the entire binding system more stable. Moreover, the rigid constraint of pipe D4 limits the twist of the molecule to reduce the twisted intramolecular charge transfer (TICT) to a certain extent, which will optimize the optical properties of the fluorophore after binding.

Then, molecular dynamics simulations were performed to verify the conformational stability of **ABTP-DPTB** after APN binding. The protein structures of APN-**ABTP-DPTB** and APN-bestatin after MD were only slightly changed after MD (Fig. 3a). The root-mean-square deviation (RMSD) curve of bestatin pre-bound to APN remained stable only for a short time, followed by a dramatic fluctuation, and finally stabilized (Fig. 3b). This indicates that the active conformation of bestatin is only maintained for a moment (Fig. 3c). After an obvious shift in its position, bestatin finally approaches stability in a new state (Fig. 3d). This suggests that the active conformation in the original crystal structure may not be stable for a

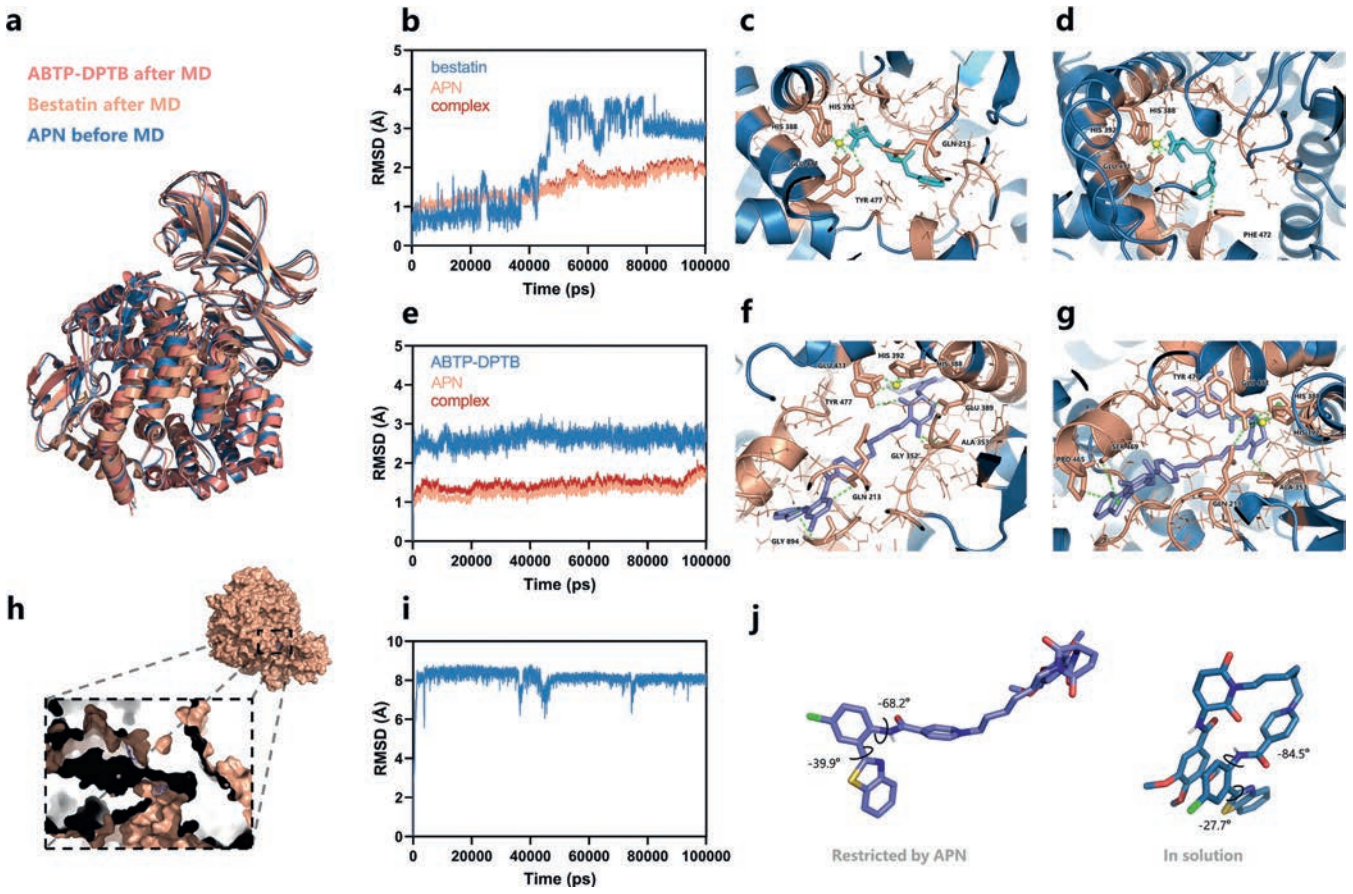

Fig. 3. Molecular dynamics simulations results. (a) The averaged complexed structures of APN-**ABTP-DPTB** (after MD, lightpink) and APN-bestatin (after MD, wheat) which were aligned to the APN without MD simulations (before MD, blue). (b, e) RMSD of the ligand, receptor and complex. (c) Hydrogen bonds between bestatin and APN before MD. (d) The binding mode between bestatin and APN after MD. (f) The binding mode between **ABTP-DPTB** and APN before MD. (g) The binding mode between **ABTP-DPTB** and APN after MD. (h) The surface map of APN and the cross-sectional view of pipe D4 combined with **ABTP-DPTB** after MD equilibrium. (i) RMSD fluctuations of **ABTP-DPTB** in the aqueous solution. (j) Conformational differences between APN-bound (purple) and free states (blue) of **ABTP-DPTB**.

long time in solution, which may lead to a decreased specificity and result in potential off-target effects [20]. Comparing the conformation before and after MD, the position of bestatin was observed to shift greatly, and the interactions between bestatin and the key residues of APN were also reduced. From the complete trajectory of MD (Video S1 in Supporting information), it can be seen intuitively that bestatin has a severer motion in the cavity inside APN, with obvious position changes, and cannot bind firmly to the active site. This phenomenon may be one of the reasons why the actual activity of bestatin is not outstanding.

The MD results of the **ABTP-DPTB** (Fig. 3e) showed that all of the RMSD curves (**ABTP-DPTB**, APN and the complex APN-**ABTP-DPTB**) were stable. And the RMSD fluctuation of protein and ligand atoms was within 1 Å, indicating that the conformation of this complex is very stable and the simulation was successful.

Comparing the conformation before (Fig. 3f) and after MD (Figs. 3g and h), the position of **ABTP-DPTB** was found basically keep steady, and the interaction between **ABTP-DPTB** and Zn^{2+} is stable. Combined with RMSD analysis results, **ABTP-DPTB** was stably bound to APN in the expected way during MD. The molecular dynamics trajectories were then analyzed and animated (Video S2 in Supporting information) to show that **ABTP-DPTB** was moving as expected within the active pocket of the APN. Then, the results of MMGBSA and MMPBSA showed that the ligand and protein had a low binding free energy (Tables S4 and S5 in Supporting information). And the hot amino acids involved in the interaction with the ligand were Glu 411, His 388, His 392, Phe 472 and Tyr 477 *etc.* (Fig. S6 in Supporting information). Compared with the effect of bestatin and APN, **ABTP-DPTB** showed superior stability and binding ability to APN. This indicates that **ABTP-DPTB** may be a more stable and effective APN targeting molecule, which can avoid potential off-target effects.

To investigate the conformation-restricted effects of APN on **ABTP-DPTB**, we calculated the state of **ABTP-DPTB** dissolved in aqueous and compared it with the APN-fixed conformation of **ABTP-DPTB**. The RMSD curve of **ABTP-DPTB** dissolved in aqueous fluctuated in a wide range (Fig. 3i), which was significantly different from the stable situ ation in the protein complex (Fig. 3e). Comparing the two key dihedral angles of the skeleton of the optical component **ABTP** after MD (Fig. 3j), it was found that the twisted state in solution is significantly enhanced (both dihedral angles are larger than the binding state in APN-**ABTP-DPTB**). Previous studies have shown that the formation of the intramolecular hydrogen bonds involved in ESIPT in fluorophore may affect the occurrence of ESIPT process [45,51]. This awards **ABTP-DPTB** different optical properties in the APN-bounded state and in the free state. According to the cross-sectional view of APN-**ABTP-DPTB** after MD, APN also plays an obvious effect in solvent isolation, which makes **ABTP-DPTB** less affected by solvent and can further promote ESIPT process. Besides, the distance between two parallel planes of **ABTP** and **DPTB** is astonishing close after MD in aqueous solution, which is obviously different from the conformation of APN-fixed. Because of the unique stack as well as the electronic difference between **ABTP** and **DPTB**, the fluorescence signal of the

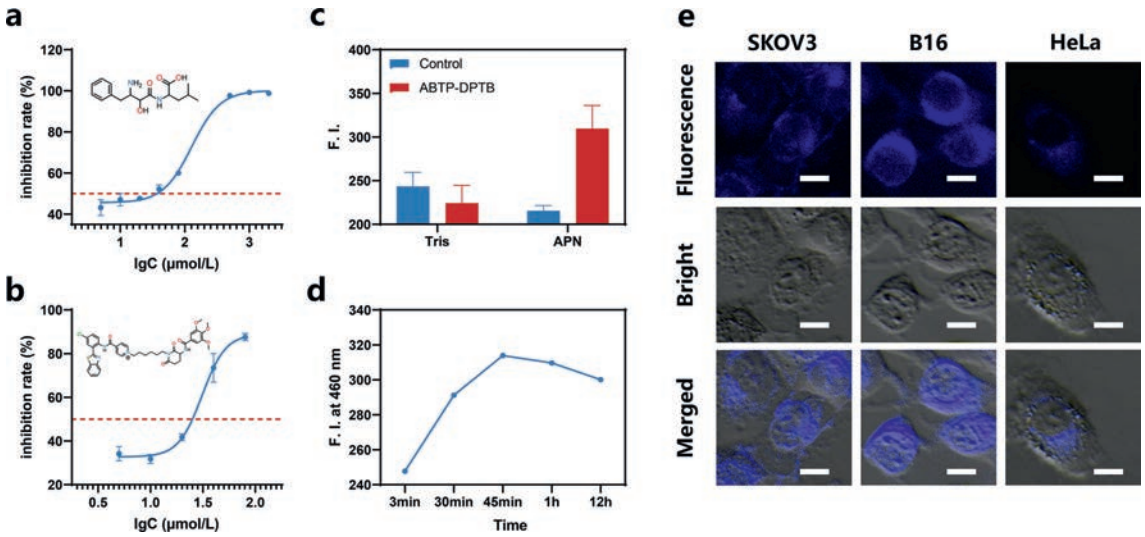

Fig. 4. Bioactivity evaluation and fluorescence imaging of **ABTP-DPTB**. (a) Inhibitory effect of bestatin on APN. (b) Inhibitory effect of **ABTP-DPTB** on APN. (c) Fluorescence intensity changes of **ABTP-DPTB** in Tris and the APN solution under 460 nm. $\lambda_{ex} = 365$ nm. Slit width (EX, EM): 9 nm. (d) Fluorescence intensity of **ABTP-DPTB** in APN at different incubation time. $\lambda_{ex} = 365$ nm, $\lambda_{em} = 460$ nm. Slit width (EX, EM): 9 nm. (e) Fluorescence microscopic images of SKOV3, B16 and HeLa cells. Cells were incubated with **ABTP-DPTB** for 15 min. Scale bar: 10 μm.

dissociative probe was further demonstrated to be quenched *via* the PET (Fig. S7 in Supporting information) [52–54], and can be restored by conformational restriction based on APN. All these results suggest that **ABTP-DPTB** has the potential to be a smart "Off–On" probe for APN.

Then the bioactivity and fluorescence imaging capability of **ABTP-DPTB** were further verified *in vitro*. The inhibitory effect results showed that the half maximal inhibitory concentration (IC_{50}) of the positive control bestatin against APN was 128.3 μmol/L (Fig. 4a), and the IC_{50} of the **ABTP-DPTB** against APN was 31.06 μmol/L (Fig. 4b). Obviously, the designed **ABTP-DPTB** showed remarkable affinity and inhibitory effect on APN, which is better than the golden-standard drug bestatin. This is was consistent with the expected results.

Besides, the **ABTP-DPTB** in APN showed much stronger fluorescence than APN and **ABTP-DPTB** (Fig. 4c). The emissions of **ABTP-DPTB** can be greatly boosted after binding with APN, which is possibly due to restriction of intramolecular motion [41]. Fluorescence microscopic images showed that **ABTP-DPTB** can rapidly image multiple cancer cells with high APN expression after incubation at 37 °C for 15 min (Fig. 4e). It indicated that **ABTP-DPTB** is qualified for detecting both cell membrane APN and the soluble APN. In addition, **ABTP-DPTB** as a specific probe can realize wash-free and rapid detection of APN with remarkable signal-noise ratio (Fig. 4c and Fig. S17 in Supporting information) [41]. Due to its high affinity for APN and obvious competitive inhibition effect, **ABTP-DPTB** theoretically has the potential for targeted long-term imaging of APN, which has been confirmed by time-dependent experiments (Fig. 4d).

In summary, this study proposed a novel quaternity design strategy for APN theranostic probe. Through this strategy, a unique "Off–On" theranostic probe, **ABTP-DPTB**, was ingeniously constructed. The "Off–On" fluorescence restoration results from inhibition of PET and enhancement of ESIPT after **ABTP-DPTB** is fixed to pipe D4, a special tubular cavity that connects the inside and outside of the APN. **ABTP-DPTB** permits the rapid, sensitive and recyclable identification as well as stable pharmacological activities of the treatment of cancers and related inflammations *via* imaging and inhibiting of APN, which is defined as cancer marker and anticancer target. Therefore, **ABTP-DPTB** is promising in the realization of early cancer diagnosis and treatment. More importantly, the proposed strategy provides a systematic reference design strategy for the development of other receptor-based theranostic probes.

Declaration of competing interest

The authors declare that they have no known competing financial interests or personal relationships that could have appeared to influence the work reported in this paper.

Acknowledgments

This work was supported by the National Natural Science Foundation of China (Nos. 82272067, 81974386, 22107123, 22003078, M-0696), the Science and Technology Foundation of Hunan Province (Nos. 2022JJ80052, 2022JJ40656), the Innovation Fund for Postgraduate Students of Central South University (Nos. 2021zzts0980, 2023ZZTS0842). The authors also acknowledge the NMR measurements by the Modern Analysis and Testing Center of CSU.

Supplementary materials

Supplementary material associated with this article can be found, in the online version, at doi:10.1016/j.cclet.2023.108948.

References

[1] H. Sung, J. Ferlay, R.L. Siegel, et al., CA Cancer J. Clin. 71 (2021) 209–249.
[2] L. Chen, Y.L. Lin, G.Q. Peng, F. Li, Proc. Natl. Acad. Sci. U. S. A. 109 (2012) 17966–17971.
[3] A.H.M. Wong, D.X. Zhou, J.M. Rini, J. Biol. Chem. 287 (2012) 36804–36813.
[4] B. Bauvois, D. Dauzonne, Med. Res. Rev. 26 (2006) 88–130.
[5] Y.P. Luan, W.F. Xu, Curr. Med. Chem. 14 (2007) 639–647.
[6] P. Mina-Osorio, Trends Mol. Med. 14 (2008) 361–371.
[7] H. Murakami, A. Yokoyama, K. Kondo, et al., Clin. Cancer Res. 11 (2005) 8674–8679.
[8] L. Pang, N. Zhang, Y. Xia, et al., Oncotarget 7 (2016) 77854–77864.
[9] F.M. Barnieh, P.M. Loadman, R.A. Falconer, Biochim. Biophys. Acta Rev. Cancer 1876 (2021) 188641.
[10] X. Li, J. Li, C.Y. Li, et al., J. Mater. Chem. B 9 (2021) 7530–7543.
[11] Y. van Hensbergen, H.J. Broxterman, R. Hanemaaijer, et al., Clin. Cancer Res. 8 (2002) 3747–3754.
[12] C.Y. Lu, M.A. Amin, D.A. Fox, J. Immunol. 204 (2020) 3–11.
[13] J.H. Kim, R. Afridi, E. Cho, et al., Mol. Cell. Proteom. 21 (2022) 100424.
[14] P. Luo, X.L. Li, Y. Gao, et al., Front. Pharmacol. 13 (2022) 904926.
[15] A. Mantovani, P. Allavena, A. Sica, F. Balkwill, Nature 454 (2008) 436–444.

[16] S.I. Grivennikov, F.R. Greten, M. Karin, Cell 140 (2010) 883–899.
[17] Y.N. Lin, M. Jiang, W.J. Chen, et al., Biomed. Pharmacother. 118 (2019) 109249.
[18] J.S. Shim, J.H. Kim, H.Y. Cho, et al., Chem. Biol. 10 (2003) 695–704.
[19] H.L. Pan, K.H. Yang, J. Zhang, et al., J. Enzym. Inhib. Med. Chem. 28 (2013) 717–726.
[20] S.A. Amin, N. Adhikari, T. Jha, J. Med. Chem. 61 (2018) 6468–6490.
[21] Y. Zhang, G.P. Zhang, Z.L. Zeng, K.Y. Pu, Chem. Soc. Rev. 51 (2022) 566–593.
[22] A. Radaelli, D. Ortiz, A. Michelotti, et al., ACS Sens. 7 (2022) 2987–2994.
[23] S. Kumaravel, G.R. Luo, S.T. Huang, et al., Biosens. Bioelectron. 203 (2022) 114212.
[24] X. Shi, Y. Deng, X.Y. Liu, et al., Biosens. Bioelectron. 208 (2022) 114049.
[25] Y. Saito, H. Yatabe, I. Tamura, et al., Sci. Adv. 8 (2022) eabj2667.
[26] S.Y. Liu, H.L. Wang, X.T. Zou, G. Nie, Sens. Actuator. B: Chem. 363 (2022) 131828.
[27] J.J. Chen, L.Q. Chen, F. Zeng, et al., Anal. Chem. 94 (2022) 8449–8457.
[28] L. Feng, Z. Tian, M. Zhang, et al., Chin. Chem. Lett. 32 (2021) 3053–3056.
[29] H.W. Liu, L.L. Chen, C.Y. Xu, et al., Chem. Soc. Rev. 47 (2018) 7140–7180.
[30] J.J. Chen, L.Q. Chen, F. Zeng, S.Z. Wu, Chem. Soc. Rev. 48 (2019) 683–722.
[31] X.Y. He, Y.H. Xu, W. Shi, H.M. Ma, Anal. Chem. 89 (2017) 3217–3221.
[32] X.Y. He, Y.M. Hu, W. Shi, et al., Chem. Commun. 53 (2017) 9438–9441.
[33] H.D. Li, Y.Q. Li, Q.C. Yao, et al., Chem. Sci. 10 (2019) 1619–1625.
[34] Y.C. Liu, C.Y. Xu, H.W. Liu, et al., Anal. Chem. 93 (2021) 6463–6471.
[35] L.Z. Chen, W. Sun, W.H. Li, et al., Anal. Methods 4 (2012) 2661–2663.
[36] L.Z. Chen, W. Sun, J. Li, et al., Org. Biomol. Chem. 11 (2013) 378–382.
[37] J. Li, L.Z. Chen, W.X. Wu, et al., Anal. Chem. 86 (2014) 2747–2751.
[38] M. Xiao, W. Sun, J.L. Fan, et al., Adv. Funct. Mater. 28 (2018) 1805128.
[39] X. Zhou, H.D. Li, C. Shi, et al., Biomaterials 253 (2020) 120089.
[40] T.N. Zang, Y.C. Xie, S. Su, et al., Angew. Chem. Int. Ed. 59 (2020) 10003–10007.
[41] Z.J. Yao, J. Dong, Y.J. Che, et al., J. Comput. Aided Mol. Des. 30 (2016) 413–424.
[42] H. Gerdes, P. Casado, A. Dokal, et al., Nat. Commun. 12 (2021) 1850.
[43] J. Dong, N.N. Wang, Z.J. Yao, et al., J. Cheminform. 10 (2018) 29.
[44] A.C. Sedgwick, L.L. Wu, H.H. Han, et al., Chem. Soc. Rev. 47 (2018) 8842–8880.
[45] C.L. Chen, Y.T. Chen, A.P. Demchenko, P.T. Chou, Nat. Rev. Chem. 2 (2018) 131–143.
[46] J.E. Kwon, S.Y. Park, Adv. Mater. 23 (2011) 3615–3642.
[47] P.W. Zhou, K. Han, Acc. Chem. Res. 51 (2018) 1681–1690.
[48] B. Feng, Y. Zhu, J. Wu, et al., Chin. Chem. Lett. 32 (2021) 3057–3060.
[49] M. Chang, C. Yan, L. Shi, et al., Chin. Chem. Lett. 33 (2022) 762–766.
[50] X. Cheng, S. Huang, Q. Lei, et al., Chin. Chem. Lett. 33 (2022) 1861–1864.
[51] V.S. Padalkar, S. Seki, Chem. Soc. Rev. 45 (2016) 169–202.
[52] H. Zhang, J.L. Fan, J.Y. Wang, et al., J. Am. Chem. Soc. 135 (2013) 11663–11669.
[53] Y. Jiao, J.Q. Yin, H.Y. He, et al., J. Am. Chem. Soc. 140 (2018) 5882–5885.
[54] Y.W. Duan, H.Y. Tang, Y. Guo, et al., Chin. Chem. Lett. 25 (2014) 1082–1086.